

A diffuse reflectance spectral imaging system for tumor margin assessment using custom annular photodiode arrays

Sulochana Dhar,^{1,*} Justin Y. Lo,² Gregory M. Palmer,³ Martin A. Brooke,¹ Brandon S. Nichols,² Bing Yu,^{2,4} Nirmala Ramanujam,² and Nan M. Jokerst¹

¹Department of Electrical and Computer Engineering, Duke University, Research Drive, Durham, NC 27708, USA

²Department of Biomedical Engineering, Duke University, Research Drive, Durham, NC 27708, USA

³Department of Radiation Oncology, Duke University, Research Drive, Durham, NC 27710, USA

⁴Currently at Department of Biomedical Engineering, University of Akron, Akron, Ohio 44325, USA

*sulochana.dhar@duke.edu

Abstract: Diffuse reflectance spectroscopy (DRS) is a well-established method to quantitatively distinguish between benign and cancerous tissue for tumor margin assessment. Current multipixel DRS margin assessment tools are bulky fiber-based probes that have limited scalability. Reported herein is a new approach to multipixel DRS probe design, which utilizes direct detection of the DRS signal by using optimized custom photodetectors in direct contact with the tissue. This first fiberless DRS imaging system for tumor margin assessment consists of a 4×4 array of annular silicon photodetectors and a constrained free-space light delivery tube optimized to deliver light across a 256 mm^2 imaging area. This system has 4.5 mm spatial resolution. The signal-to-noise ratio measured for normal and malignant breast tissue-mimicking phantoms was 35 dB to 45 dB for $\lambda = 470 \text{ nm}$ to 600 nm .

©2012 Optical Society of America

OCIS codes: (170.3890) Medical optics instrumentation; (040.1240) Arrays.

References and links

1. N. Rajaram, T. H. Nguyen, and J. W. Tunnell, "Lookup table-based inverse model for determining optical properties of turbid media," *J. Biomed. Opt.* **13**(5), 050501 (2008).
2. L. G. Wilke, J. Q. Brown, T. M. Bydlon, S. A. Kennedy, L. M. Richards, M. K. Junker, J. Gallagher, W. T. Barry, J. Geradts, and N. Ramanujam, "Rapid noninvasive optical imaging of tissue composition in breast tumor margins," *Am. J. Surg.* **198**(4), 566–574 (2009).
3. D. Contini, F. Martelli, and G. Zaccanti, "Photon migration through a turbid slab described by a model based on diffusion approximation. I. Theory," *Appl. Opt.* **36**(19), 4587–4599 (1997).
4. G. M. Palmer and N. Ramanujam, "Monte Carlo-based inverse model for calculating tissue optical properties. Part I: Theory and validation on synthetic phantoms," *Appl. Opt.* **45**(5), 1062–1071 (2006).
5. L. Wang, S. L. Jacques, and L. Zheng, "MCML--Monte Carlo modeling of light transport in multi-layered tissues," *Comput. Methods Programs Biomed.* **47**(2), 131–146 (1995).
6. N. Lue, J. W. Kang, C.-C. Yu, I. Barman, N. C. Dingari, M. S. Feld, R. R. Dasari, and M. Fitzmaurice, "Portable optical fiber probe-based spectroscopic scanner for rapid cancer diagnosis: a new tool for intraoperative margin assessment," *PLoS ONE* **7**(1), e30887 (2012).
7. F. T. Nguyen, A. M. Zysk, E. J. Chaney, J. G. Kotynek, U. J. Oliphant, F. J. Bellafiore, K. M. Rowland, P. A. Johnson, and S. A. Boppart, "Intraoperative evaluation of breast tumor margins with optical coherence tomography," *Cancer Res.* **69**(22), 8790–8796 (2009).
8. SUROS, "New method for breast cancer diagnosis," 2003, <http://www2.prnewswire.com/cgi-bin/stories.pl?ACCT=104&STORY=/www/story/11-25-2003/0002065545&EDATE=>.
9. L. Jacobs, "Positive margins: the challenge continues for breast surgeons," *Ann. Surg. Oncol.* **15**(5), 1271–1272 (2008).
10. T. L. Huston, R. Pigalarga, M. P. Osborne, and E. Tousimis, "The influence of additional surgical margins on the total specimen volume excised and the reoperative rate after breast-conserving surgery," *Am. J. Surg.* **192**(4), 509–512 (2006).
11. G. C. Balch, S. K. Mithani, J. F. Simpson, and M. C. Kelley, "Accuracy of intraoperative gross examination of surgical margin status in women undergoing partial mastectomy for breast malignancy," *Am. Surg.* **71**(1), 22–27, discussion 27–28 (2005).

12. T. M. Bydlon, S. A. Kennedy, L. M. Richards, J. Q. Brown, B. Yu, M. K. Junker, J. Gallagher, J. Geradts, L. G. Wilke, and N. Ramanujam, "Performance metrics of an optical spectral imaging system for intra-operative assessment of breast tumor margins," *Opt. Express* **18**(8), 8058–8076 (2010).
13. H. L. Fu, B. Yu, J. Y. Lo, G. M. Palmer, T. F. Kuech, and N. Ramanujam, "A low-cost, portable, and quantitative spectral imaging system for application to biological tissues," *Opt. Express* **18**(12), 12630–12645 (2010).
14. J. Y. Lo, B. Yu, H. L. Fu, J. E. Bender, G. M. Palmer, T. F. Kuech, and N. Ramanujam, "A strategy for quantitative spectral imaging of tissue absorption and scattering using light emitting diodes and photodiodes," *Opt. Express* **17**(3), 1372–1384 (2009).
15. B. Yu, J. Y. Lo, T. F. Kuech, G. M. Palmer, J. E. Bender, and N. Ramanujam, "Cost-effective diffuse reflectance spectroscopy device for quantifying tissue absorption and scattering in vivo," *J. Biomed. Opt.* **13**(6), 060505 (2008).
16. S. Duun, R. G. Haahr, O. Hansen, K. Birkelund, and E. V. Thomsen, "High quantum efficiency annular backside silicon photodiodes for reflectance pulse oximetry in wearable wireless body sensors," *J. Micromech. Microeng.* **20**(7), 075020 (2010).
17. J. Y. Lo, J. Q. Brown, S. Dhar, B. Yu, N. M. Jokerst, and N. Ramanujam, "Wavelength optimization for quantitative spectral imaging of breast tumor margins," submitted to PLoS ONE.
18. J. Y. Lo, S. Dhar, B. Yu, M. A. Brooke, T. F. Kuech, N. M. Jokerst, and N. Ramanujam, "Diffuse reflectance spectral imaging for breast tumor margin assessment," *Proc. SPIE* **8214**, 821407 (2012).
19. S. Wolf and R. N. Tauber, *Silicon Processing for the VLSI Era, Vol. 1: Process Technology* (Lattice, 1999).
20. M. J. Kerr, J. Schmidt, A. Cuevas, and J. H. Bultman, "Surface recombination velocity of phosphorus-diffused silicon solar cell emitters passivated with plasma enhanced chemical vapor deposited silicon nitride and thermal silicon oxide," *J. Appl. Phys.* **89**(7), 3821–3826 (2001).
21. S. Dhar, J. Y. Lo, B. Yu, M. A. Brooke, N. Ramanujam, and N. M. Jokerst, "Custom annular photodetector arrays for breast cancer margin assessment using diffuse reflectance spectroscopy," in *2011 IEEE Biomedical Circuits and Systems Conference (BioCAS)* (IEEE, 2011), pp. 440–443.
22. S. Dhar, J. Y. Lo, B. Yu, T. Tyler, M. A. Brooke, T. F. Kuech, N. Ramanujam, and N. M. Jokerst, "A custom wide-field spectral imager for breast cancer margin assessment," in *2011 IEEE Photonics Conference (PHO)* (IEEE, 2011), pp. 798–799.
23. Asahi Spectra, "MAX-302 xenon light source 300W technical information," http://www.gmp.ch/htmlarea/pdf/asahi_pdf/max302techinfo.pdf.
24. E. Hecht, *Optics*, 4th ed. (Addison Wesley, 2001).
25. Texas Instruments, "IVC102 precision switched integrator transimpedance amplifier," <http://www.ti.com/product/ivc102>.
26. PICAXE microcontroller, available from <http://www.picaxe.com/>.
27. T. M. Bydlon, W. T. Barry, S. A. Kennedy, J. Q. Brown, J. Gallagher, L. G. Wilke, J. Geradts, and N. Ramanujam, "Advancing optical imaging for breast margin assessment: an analysis of excisional time, cautery, and and patent blue dye on underlying sources of contrast," PLoS ONE (to be published).
28. G. M. Palmer and N. Ramanujam, "Monte Carlo-based inverse model for calculating tissue optical properties. Part I: Theory and validation on synthetic phantoms," *Appl. Opt.* **45**(5), 1062–1071 (2006).
29. M. Born and E. Wolf, *Principles of Optics: Electromagnetic Theory of Propagation, Interference and Diffraction of Light*, 6th ed (Pergamon, Oxford, 1980).
30. T. Bååk, "Silicon oxynitride; a material for GRIN optics," *Appl. Opt.* **21**(6), 1069–1072 (1982).

1. Introduction

Diffuse reflectance from turbid media such as biological tissue is sensitive to the absorption and scattering of the constituents of these media. In the case of biological tissue, diffuse reflectance spectroscopy (DRS) can be used to look for spectral signatures of molecules such as oxy-hemoglobin, deoxy-hemoglobin, collagen, and beta-carotene [1,2], for example. DRS performed with well-defined illumination and collection geometries and coupled with physically based light transport models can be used to quantitatively extract tissue optical properties (absorption and scattering) [3–5]. This information can then be used to develop appropriate decision tree models to discern between healthy and cancerous tissue [2,6].

One application for which DRS has been investigated is intra-operative tumor margin assessment for breast conserving surgery (BCS) [2,6,7]. Over 200,000 women are diagnosed with breast cancer annually in the United States, and 50%–75% of these women are eligible for BCS [8]. Of the women undergoing BCS, 20%–70% return for a re-excision surgery due to incompletely removed tumor in the first surgery [9–11]. The goal of DRS imaging in this context is to reduce the re-excision rate.

Our group has developed a bench-top tissue imaging system, based on quantitative DRS, for intra-operative tumor margin assessment. Briefly, the bench-top system consists of a xenon arc lamp, an imaging spectrograph, and a cooled CCD camera to image the DRS spectra collected by an 8-channel fiber optic probe [12]. The 8-channel fiber optic probe

consists of 8 individual fiber probes, each composed of illumination fibers surrounded by collection fibers. An inverse Monte-Carlo model, developed by Palmer et al. [4], is used to extract tissue optical properties (absorption coefficient and reduced scattering coefficient) using the DRS spectra collected by the bench-top system. The system surveys the target region of interest over a wavelength range of 450-600 nm and a sensing depth of 2 mm (the criterion for clear margins) to provide quantitative maps of oxy-hemoglobin, deoxy-hemoglobin, beta-carotene and scattering. A classification model was developed using a combination of these endpoints to detect positive tumor margins with a sensitivity of 79.4% (i.e., percentage of correctly detected positive margins), and specificity of 66.7% (i.e., percentage of correctly detected negative margins) from a 48 patient cohort, demonstrating its potential to significantly reduce re-excision surgeries [2]. However, this system costs \$50,000, has a footprint of 2 m \times 1 m, and is only capable of coarse 8-pixel imaging [12,13]. In addition, the ability to rapidly assess large margin areas is key in the context of breast cancer imaging, since excised breast tissue areas can be as large as 20 cm². Therefore, there is a need for a low-cost, fast, compact, portable spectral imaging system with multi-pixel, large-area probes for breast tumor margin assessment inside the surgical suite, where space and time are at a premium.

In an effort to reduce the complexity and footprint of this bench-top system, a more compact system was developed where DRS spectra were sampled using a xenon lamp followed by eight discrete wavelength filters. It was demonstrated that optical properties could be extracted with low errors using the inverse Monte Carlo model, with eight wavelengths of light as opposed to 81 wavelengths used in the bench-top system [14]. In addition, an array of mechanically drilled commercial silicon photodiodes was developed to achieve Si photodiode-based collection, and fibers were epoxied to the drilled photodiode apertures to achieve fiber-based illumination in the DRS probe [13]. This system obviated the need to use an imaging spectrograph and a 2D CCD for obtaining spectral information; components that significantly added to the complexity and foot-print of the bench-top system. The drilled photodiodes with epoxied fibers replaced previous illumination/collection fiber probes, however pixel spacing was still limited by commercial photodiode packaging and this system had limited scalability and resolution.

Here, we report the design, optimization, fabrication, and characterization of a multipixel DRS imaging system using a custom photodetector array and constrained free space illumination. This system enables fiberless illumination of tissue sites and collection of DRS signals by the use of an array of custom annular silicon photodetectors (PDs), which directly contact the tissue. Illumination from a filtered xenon lamp is incident upon an aperture in the center of each of the annular PDs. After the signal enters tissue and is diffusely reflected, the DRS signal is collected by the annular PD surrounding the aperture. This illumination-collection geometry has been shown to have the highest SNR for contact-based DRS [14,15]. While annular silicon PDs with back illumination have been used in applications such as pulse oximetry [16], these systems utilize single PDs and have two-wavelength interrogation. This report utilizes an array of sixteen annular PD pixels, arranged in a 4 \times 4 format and eight discrete wavelengths to obtain DRS spectral information from thick tissues.

2. System description

The schematic of the overall system is shown in Fig. 1(a). Figure 1(b) shows a photograph of the custom compact spectral imaging system, and Fig. 1(c) shows the contact imaging probe. The system reported herein consisted of a xenon arc lamp (MAX-302, Asahi Spectra) with eight discrete wavelength filters as the illumination source, a sixteen pixel imaging array composed of customized annular silicon photodiodes, a quartz light delivery tube that enables free space illumination of tissue sites, a custom eight-channel integrating transimpedance amplifier (ITIA) circuit for photodiode readout, and a custom switch box connected to the eight channel ITIA circuit that enables per-pixel amplification and readout of all sixteen pixels in the array. Each of these system components is controlled by a LabVIEW program running on a laptop computer.

Spectral information was collected by making successive diffuse reflectance measurements with each of the eight wavelength band pass filters with center wavelengths at 470 nm, 480 nm, 490 nm, 500 nm, 510 nm, 560 nm, 580 nm, and 600 nm [17]. Each filter was mounted on an eight-slot filter wheel inside the xenon arc lamp and had a $\Delta\lambda = 10$ nm full width at half max. Light from the xenon lamp passed through one filter at a time, and exited the lamp through a 5.2 mm diameter, 0.57 numerical aperture (N.A.) fiber bundle. The fiber bundle was connected to one end of the quartz light delivery tube and the custom imager was mounted on the distal end of the quartz tube, as shown in Fig. 1(a) and Fig. 1(c). The imager consisted of sixteen annular silicon photodiodes with 2.5 mm outer diameter (O.D.), and 0.75 mm inner diameter (I.D.) central apertures. The center-to-center spacing of the array pixels was 4.5 mm. The O.D. and I.D. of the PDs were designed to achieve a sensing depth of 0.4–2 mm in breast tissues [18]. Light traveled from the fiber bundle, through free space in the quartz tube, through the PD apertures. The specimen under investigation was placed in contact with the imager. Light traveling through the PD apertures illuminated the tissue sites, and diffusely reflected light from the specimen was incident upon the detection area of the annular PDs. This diffusely reflected light generated carriers in the photodiodes, read as photocurrent by the readout circuit.

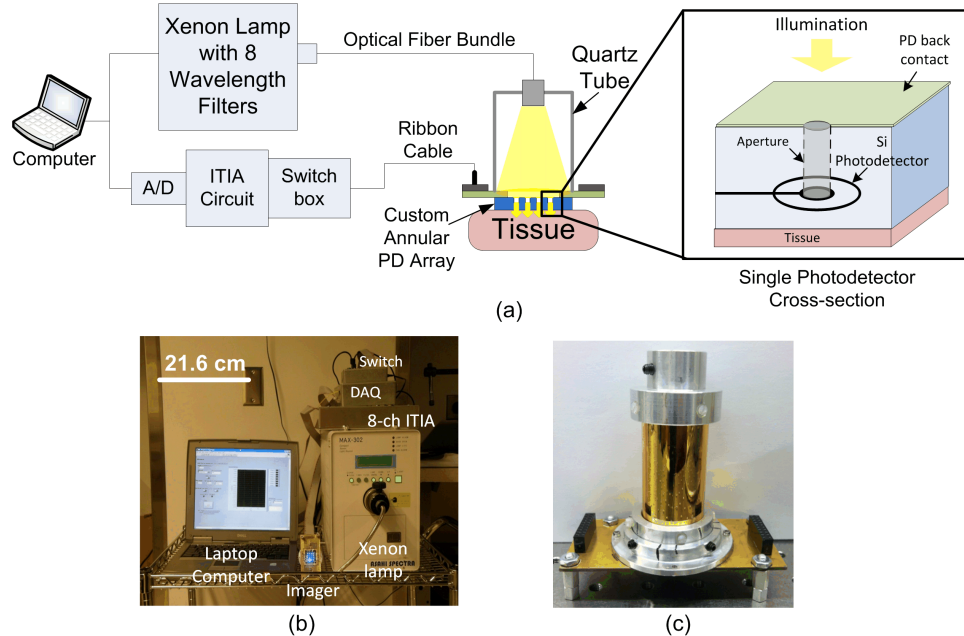


Fig. 1. (a) Schematic of the DRS imaging system and cross-section view of a single PD in the array (b) Photograph of DRS imaging system (c) Photograph of the customized DRS imaging probe with a fiberless quartz light delivery tube and an annular custom silicon photodiode array.

3. System development and optimization

3.1. Custom annular photodetector array fabrication and characterization

Fabrication of the custom-imaging array began with an n-type epitaxial Si wafer: 7 μm n-Si (epitaxial, P doped, 5-9 $\Omega\text{-cm}$) on 600 μm n-Si (substrate, Sb doped, 0.025-0.045 $\Omega\text{-cm}$). The Sb-doped substrate side of the wafer was coated with a phosphorous doped spin-on-glass (Emulsitone Phosphorosilica film $5 \times 10^{20} \text{ cm}^{-3}$) and annealed to form an n + back contact layer. A 150 nm thick SiO_2 layer was grown using thermal oxidation on the epilayer and was patterned to define the active area of each PD. A boron doped spin-on-glass (Emulsitone Borosilicafilm $5 \times 10^{19} \text{ cm}^{-3}$) was spin coated on the front-side epitaxial layer of the wafer

and annealed to form the pn junctions. Since the diffusion coefficient of boron is lower in SiO₂ compared to Si [19], the patterned oxide layer served as a diffusion mask to dope only the active areas of the PDs. The top dual-ring aluminum ohmic contact was patterned using UV lithography and an Al/Pt stack was deposited as the blanket ohmic back contact. A 0.75 mm diameter 600 μ m deep aperture was patterned in each PD using UV lithography and etched using deep reactive-ion etching (Bosch process, SPTS Pegasus). Finally, a 52 nm thick PECVD silicon nitride (SiN) layer was deposited on the PDs as an anti-reflection (AR) coating. The SiN layer also served to passivate the front surface of the PDs, thereby reducing the front surface recombination velocity [20]. The fabricated imaging array was wire-bonded to a patterned gold-coated FR4 board to enable PD current readout.

Characterization of the imaging array was performed using the fiber-coupled Asahi lamp with 8 wavelength filters as an illumination source to measure surface normal spectral response of the fabricated PDs. Light from a fiber bundle was incident on each PD in the surface normal configuration, and the resulting photocurrent in each PD was measured using a source-measurement unit (Keithley SMU-4200). Power at the output of the fiber bundle was measured using a calibrated Si photodetector head (Thorlabs S120A) connected to an optical power meter (Thorlabs PM100) to calculate the PD spectral response. A 3D simulation was performed in Silvaco Atlas® to theoretically estimate the surface normal spectral response and junction depth of the fabricated PDs. The Silvaco model used the dopant concentrations and epilayer thickness of the starting wafer. A complementary error-function profile was assumed for boron diffusion with boron surface concentration equal to $5 \times 10^{19} \text{ cm}^{-3}$. Figure 2(a) shows the average measured surface normal spectral response for 15 PDs in the array shown in Fig. 2(b). One pixel in the array had an unusually low responsivity of 1 mA/W to 3 mA/W, and was not included in the average. The simulated spectral response for a junction depth of 700 nm agrees well with the measured responsivity. The average responsivity for the 15 PDs was measured to be 0.13 A/W to 0.3 A/W for $\lambda = 400 \text{ nm}$ to 600 nm . The dark current density of the fabricated PDs was measured to be 14.56 pA/mm² to 44.8 pA/mm².

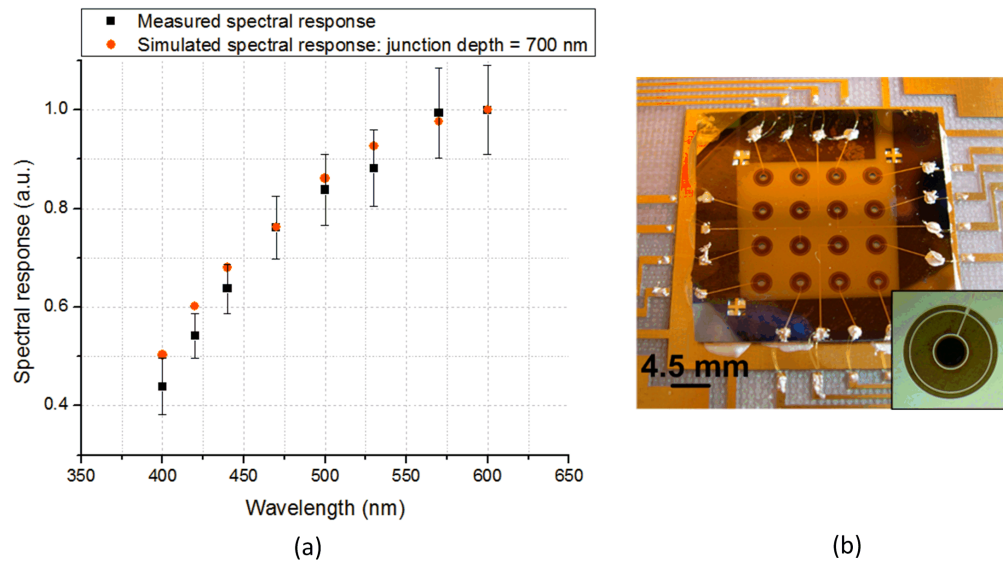


Fig. 2. (a) Measured and predicted spectral response of fabricated 4×4 array of silicon PDs. Error bars are $\pm 1\sigma$. (b) Photograph of fabricated and packaged array (inset) Photomicrograph of one pixel in the annular PD array.

3.2. Light delivery design and characterization

Light was delivered to individual test sites through central apertures in the fabricated PDs to maximize the SNR of the resulting diffuse reflectance signal [15]. While our previously

reported diffuse reflectance imaging systems have utilized individual fibers or fiber bundles to illuminate each tissue site, these systems have been limited to less than 10 illumination sites per image, and pixel spacings greater than 7 mm [12,13]. As pixel to pixel spacing decreases, and in addition, imaging area increases, illuminating each tissue site with a fiber becomes increasingly unwieldy. One way towards a more scalable light delivery system without fiber-based illumination is by using a light delivery tube coupled to a single source fiber bundle, to deliver light to all of the pixels of the array.

The system reported herein uses a metalized quartz tube, optimized in length and diameter, to ensure sufficient power throughput through PD apertures and uniformity across all pixels. This optimized tube replaced a suboptimal Al tube used in previous experiments [21,22]. The diameter of the fabricated array is 22.6 mm, so a 27 mm I.D./30 mm O.D. quartz tube was selected, in order to accommodate the array in the center of the tube for illumination. The length and diameter of the tube were simulated to utilize rays reflected from the metalized tube to enhance light throughput and uniformity across the array. Simulations were performed using a commercially available ray tracing software, ZEMAX®, to estimate light throughput and uniformity. The ZEMAX® model simulated the N.A. (0.57) of the source fiber bundle and the intensity distribution across the source fiber bundle [23]. A tube diameter larger than 30 mm O.D. increases the length of the tube required to utilize reflections from the metalized walls of the tube without any improvement in light throughput. Therefore, in order to limit the size of the probe, a tube diameter of 27 mm I.D./30 mm O.D. was chosen. Optimization of the tube length, for the chosen tube diameter, is shown in Fig. 3(a) for $\lambda = 470$ nm and 600 nm. It should be noted that corner pixel illumination is a challenge due to the thickness of the PD

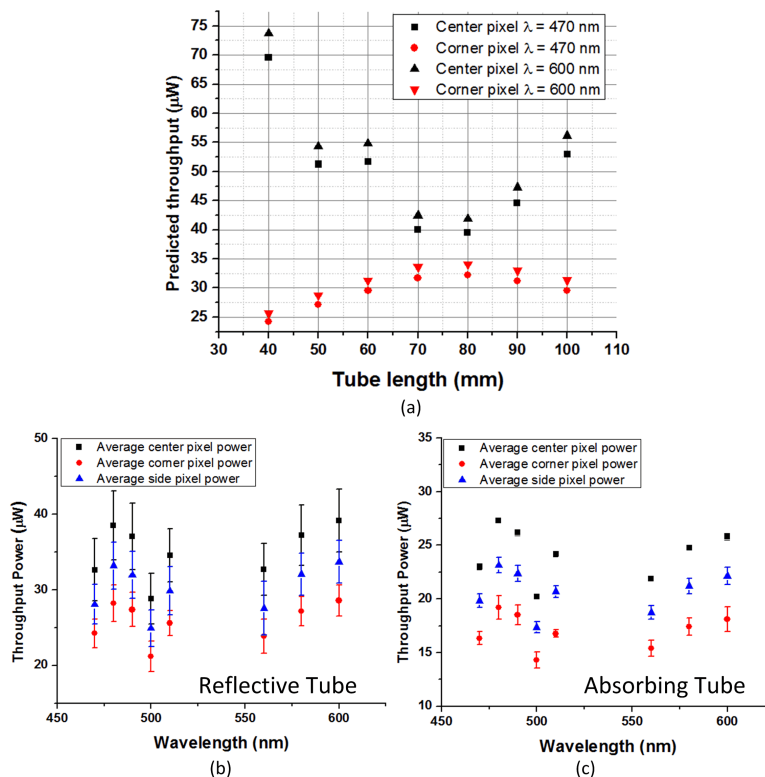


Fig. 3. (a) Power throughput through PD apertures using a reflective tube for light delivery, simulated in ZEMAX® (b) Average measured power throughput for 4 center pixels, 4 corner pixels and 8 side pixels using a 70 mm long reflective tube (c) Average measured power throughput for 4 center pixels, 4 corner pixels and 8 side pixels using a 70 mm long absorbing tube. Error bars are $\pm 1\sigma$, and the spectral content reflects that of the source.

array and their distance from the center of the fiber bundle. A tube length of 70 mm is optimum for corner pixel throughput and uniformity between corner and center pixel light throughput. The simulated corner-to-center pixel light throughput ratio was 0.78 (i.e., 78% uniformity) for a 70 mm tube length.

The quartz tube was coated with Ag (2500 Å)/Au (2500 Å) using e-beam evaporation, due to high reflectivity of Ag for $\lambda = 470$ nm to 600 nm [24]. The measured optical power through the PD apertures is shown in Fig. 3(b). The measured corner-to-center pixel uniformity was 73.5%, and was within 5% of the value predicted by ZEMAX®.

Power throughput through the PD apertures was also measured for a quartz tube identical in dimensions to the reflective tube, but coated on the inside with absorbing black paint. While using an absorbing tube reduces light throughput by 30%, as shown in Fig. 3(c), the angular distribution of rays emerging from the PD apertures is smaller for the absorbing tube compared to the reflective tube (due to the absence of reflected rays in the absorbing tube). The angular distribution of rays has an impact on pixel-to-pixel optical crosstalk, with increasing angular distribution leading to higher levels of crosstalk, which has also been studied herein.

3.3. Custom interface circuit design and development

Eight parallel Integrating Transimpedance Amplifiers (ITIAs) were built using commercial parts [25]. A digitally controlled mechanical relay switch box was used to connect the 8 amplifiers to the 16 pixels, 8 at a time. A low cost microcontroller [26] was used to control the amplifier operation and interface to a measurement computer and data collection system. The interface circuit was programmable for different integration times, and this system achieved an SNR of better than 55 dB for currents greater than 4 nA with 100 ms integration time. The entire resulting interface system, including ITIAs, switch box, and data acquisition, occupies a volume that is significantly smaller than the volume occupied by the xenon lamp.

4. Experimental system characterization

Experimental characterization of the system was conducted to quantify system signal-to-noise ratio (SNR) and optical crosstalk in tissue. Optical crosstalk in tissue is the diffuse reflectance signal generated in a pixel due to tissue illumination from neighboring pixel apertures. System SNR and crosstalk were measured for two breast tissue mimicking phantoms. The phantoms were a mixture of methemoglobin (absorber) and polystyrene spheres (scatterers) dissolved in deionized water. The phantoms were prepared with known optical properties similar to normal and malignant breast tissue. The normal tissue phantom is characterized by low absorption and high scattering properties (averaged $\mu_a = 0.56 \text{ cm}^{-1}$ and $\mu_s' = 11.9 \text{ cm}^{-1}$), whereas the simulated malignant tissue has relatively higher absorption and lower scattering (averaged optical properties $\mu_a = 5.42 \text{ cm}^{-1}$ and $\mu_s' = 3.43 \text{ cm}^{-1}$). Because the goal is to study the effect of optical crosstalk in tissue, the worst-case and best-case scenarios for optical crosstalk in clinically relevant tissue were simulated based on previously measured breast tissue data [27]. The assumption is that any mean or median normal and malignant tissue types would not

Table 1. Optical properties of tissue phantoms

Wavelength (nm)	Benign breast tissue phantom [27]		Cancerous breast tissue phantom [27]	
	$\mu_a (\text{cm}^{-1})$	$\mu_s' (\text{cm}^{-1})$	$\mu_a (\text{cm}^{-1})$	$\mu_s' (\text{cm}^{-1})$
470	0.6646	11.1447	6.5732	3.1904
480	0.6465	10.9422	6.3943	3.1324
490	0.6603	10.8254	6.5300	3.0990
500	0.6644	10.7530	6.5708	3.0783
510	0.6307	10.6877	6.2380	3.0596
560	0.4254	10.0198	4.2068	2.8684
580	0.4207	9.7991	4.1611	2.8052
600	0.3013	9.6849	2.9800	2.7725

exhibit as much optical crosstalk, and it is important to characterize and model the crosstalk in normal and malignant tissues to be able to ultimately classify them. The wavelength-dependent optical properties of the tissue-simulating phantoms are listed in Table 1.

4.1. SNR

The system SNR was calculated using 30 repeated measures at each wavelength of diffuse reflectance signal photocurrent generated in each PD when the imaging array was placed in contact with the tissue phantom. The SNR in dB is defined as $20\log_{10}(I_{\text{mean}}/\sigma)$, where I_{mean} is the mean of 30 repeated measures, and σ is the corresponding standard deviation. Unfortunately, in the course of imaging array characterization, two pixels in the imaging array became unresponsive due to disconnected wire-bonds, but these poorly responding pixels are simple packaging and yield problems that will be addressed in future work. Figure 4(a) and Fig. 4(b) show the average SNR for 13 out of 16 pixels in the imaging array (excluding the two unresponsive pixels, and one pixel with low responsivity), measured from the normal tissue phantom tested with the reflective tube for light delivery, and for a malignant tissue phantom tested with the absorbing tube for light delivery.

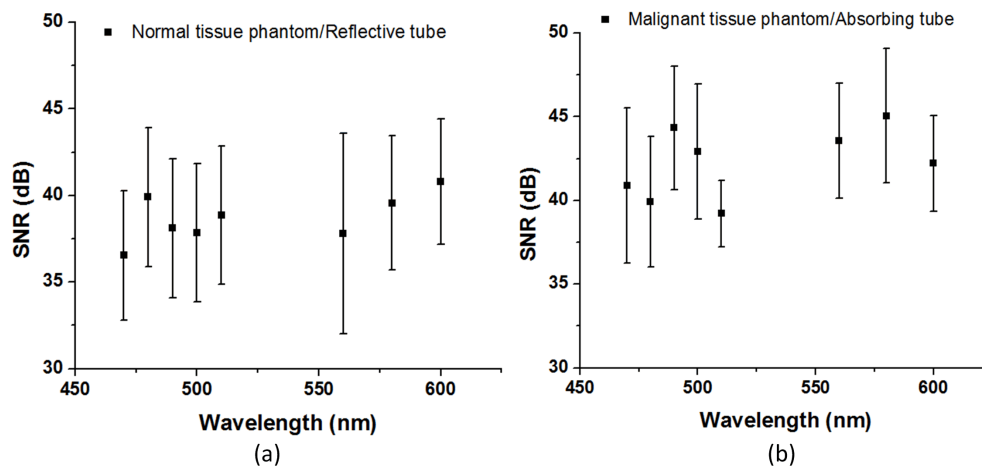


Fig. 4. (a) Calculated SNR for normal tissue phantom tested with a reflective tube for light delivery using 10 ms integration time in ITIA read-out circuit; (b) Calculated SNR for malignant tissue phantom tested with an absorbing tube for light delivery using 100 ms integration time in ITIA readout circuit. Error bars are $\pm 1\sigma$ for the mean SNR across 13 pixels.

It is observed from Fig. 4(a) and Fig. 4(b) that higher SNR is achieved for the malignant tissue phantom measured using the absorbing tube in spite of lower signal levels compared to normal tissue phantom (less absorbing) measured using the reflective tube (higher throughput). These higher signal levels from the reflective tube dictated shorter integration times, to avoid saturating the TIA. The higher SNR from the absorbing tube is likely due to lower σ as a result of averaging of the lamp noise with the longer integration time (100 ms).

4.2. System crosstalk measurement and analysis

In the design of fast multipixel DRS probes, it is important to understand the trade-off between resolution (pixel to pixel spacing) and crosstalk. Optical crosstalk in tissue refers to the photocurrent generated in a PD pixel due to illumination of tissue from neighboring PD apertures. A smaller pixel to pixel spacing (i.e., higher resolution) results in higher crosstalk. As the pixel to pixel spacing (i.e., PD spacing) in the imaging array decreases, more photons can travel from through tissue from neighboring PD apertures. This may reduce contrast between two neighboring PD pixels because the photons detected by a PD can no longer be correlated to the illumination aperture of the same PD. Hence, optical crosstalk in tissue is an important system parameter for multipixel DRS imaging systems. In this report, crosstalk is

defined as the percentage of total diffuse reflectance signal generated at a pixel due to photons traveling through tissue from neighboring illuminated PD apertures. In previously reported DRS systems, crosstalk comprised less than 10% of the total measured diffuse reflectance signal at each pixel. Crosstalk can be reduced by increasing center-to-center pixel spacing, as in these previously reported systems, which had a center-to-center pixel spacing greater than or equal to 7 mm [12,13], in contrast to the 4.5 mm center-to-center pixel spacing reported herein.

Optical crosstalk in tissue was simulated for the probe geometry reported herein, using a scalable forward Monte-Carlo model previously described [28]. Photon launch trajectories were first simulated by modeling the illumination geometry in ZEMAX®. This provided the ray angles emerging through each aperture in the PD array. The optical power through each aperture in the array was measured and used to model the relative intensity of each aperture in the array. The ray angles, along with the relative aperture intensities, were used in a set of 16 different baseline simulations, corresponding to each aperture in the array. The boundary conditions were assumed to be semi-infinite, with a 52 nm thick layer SiN coating over silicon, whose reflectivity was calculated using the method described in Born and Wolf [29]. All simulations were performed using optical properties of SiN calculated for $\lambda = 500$ nm [30]. The signal generated at a PD due to photons traveling through its own illumination aperture was determined by calculating the collected fraction hitting each detector when its own aperture was illuminated, while the signal from the illumination of neighboring apertures was calculated by summing the contribution from the remaining 15 apertures.

Figure 5(a) and Fig. 5(b) show the simulated optical crosstalk for a center pixel of the imaging array using a reflective tube, and an absorbing tube, respectively. The contour lines represent $\log_{10}(\text{crosstalk})$, and red and green data points represent the theoretical optical properties of malignant and normal tissue mimicking phantoms (listed in Table 1) at the eight wavelengths of interest. Table 1 and Fig. 5 demonstrate that optical crosstalk increases from 470 nm to 600 nm, because absorption decreases with increasing wavelength, and thus photons at longer wavelengths travel further in the tissue. Overall, higher crosstalk is expected in normal tissue, since absorption is lower than in malignant tissue.

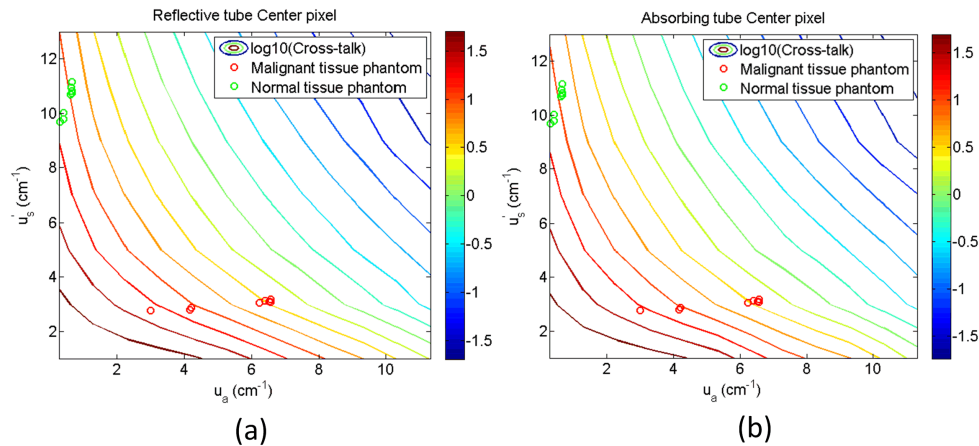


Fig. 5. Contour lines of simulated crosstalk as a function of tissue optical properties for the probe geometry reported herein. This crosstalk was simulated using a forward Monte-Carlo model for the center pixel of the imaging array illuminated using (a) a reflective tube and (b) an absorbing tube.

The crosstalk in the system was experimentally determined by measuring the diffuse reflectance from the two tissue phantoms listed in Table 1 while using beam blocking material to block illumination for all PD apertures except the PD pixel under consideration, i.e., only one PD aperture was illuminated, and the photocurrent from all PD pixels was measured. Beam blocking material (Thorlabs TB4 sliced to 0.6 mm thickness) with a single aperture

allowed illumination of only the PD pixel under consideration. This provided a measure of the diffuse reflectance signal at the illuminated PD pixel in the absence of any photons from neighboring PD apertures. A second measurement was made by removing the beam block to illuminate all PD apertures simultaneously, while keeping the rest of the optical set-up unchanged. The two successive measurements were used to calculate the crosstalk using the following equation:

$$\text{Crosstalk}(\%) = \frac{I_{ph, API} - I_{ph, SPI}}{I_{ph, API}} \times 100,$$

where, $I_{ph, API}$ is the measured PD photocurrent with all photodetector apertures illuminated, and $I_{ph, SPI}$ is the measured PD photocurrent with a single photodetector pixel illuminated.

Figure 6(a) and Fig. 6(b) show the worst case scenarios: the center and side pixels with a reflective tube (i.e., the tube that results in reflected rays forming large angles with the axis of the tube, to emerge from PD apertures) and the absorbing tube for normal, low absorption tissue. Although the absorbing tube results in lower optical throughput, with longer ITIA

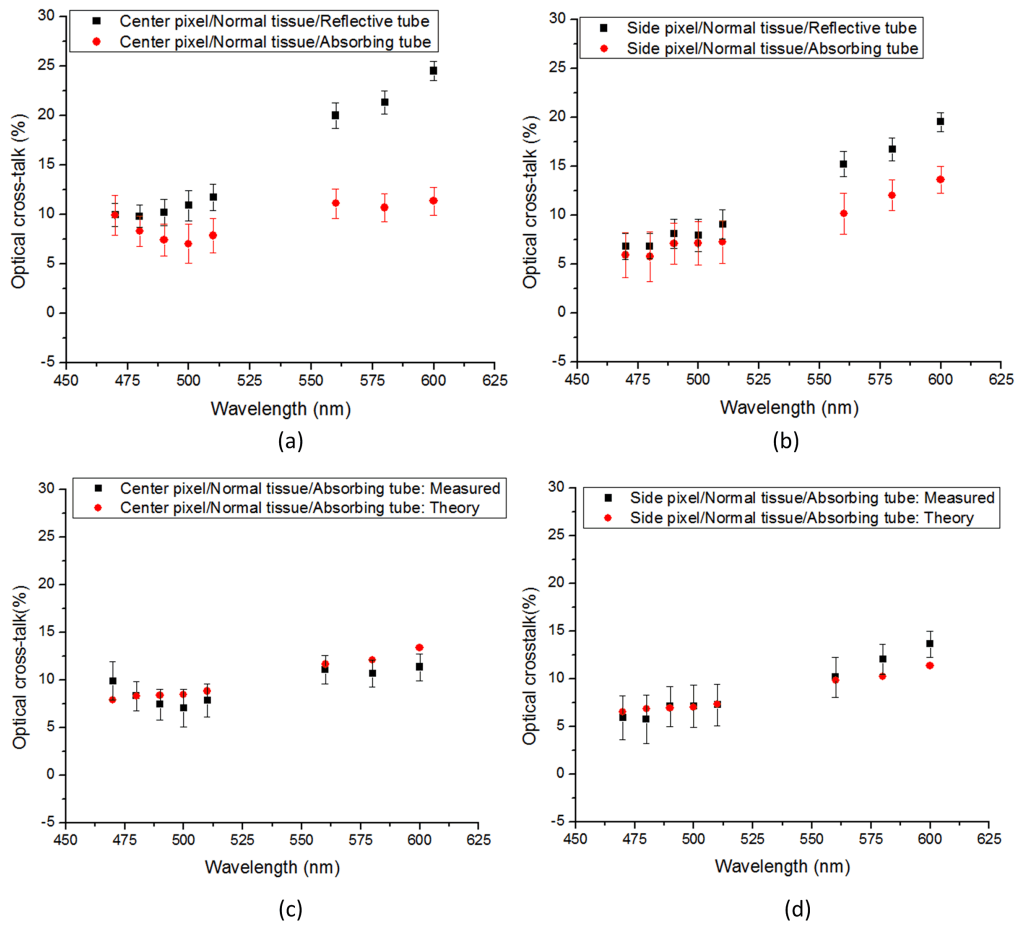


Fig. 6. (a) Crosstalk measured for a center pixel of the imaging array on normal tissue mimicking phantom using a reflective and an absorbing tube; (b) Crosstalk measured for a side pixel of the imaging array on normal tissue mimicking phantom using a reflective and an absorbing tube; (c) Measured and simulated crosstalk for a center pixel of the imaging array on a normal tissue mimicking phantom using an absorbing tube; (d) Measured and simulated crosstalk for a side pixel of the imaging array on a normal tissue mimicking phantom using an absorbing tube.

integration time, the SNR and optical crosstalk are superior for the absorbing tube. Figure 6(c) and Fig. 6(d) show a comparison between the theoretically predicted crosstalk and experimentally observed crosstalk for the absorbing tube (longer integration time) for the center (c) and side (d) pixels shown in Fig. 6 (a) and Fig. 6(b), respectively. Two full data sets were measured for the center pixel, which varied by 6%-7% in magnitude, but followed the same trend (i.e., higher crosstalk with reflective tube, increasing crosstalk at longer wavelengths). The data set with best theoretical agreement is shown in Fig. 6(a) and Fig. 6(c). The good agreement between the theoretical and measured crosstalk validates the model, and offers the potential for this model to be used in future simulations to predict the crosstalk for imagers with different pixel configurations.

5. Comparison to previously developed fiber based DRS imaging systems

Multipixel fiber-based illumination and collection is a faster method than single probe scanning, but poses a challenge in scaling imaging probes for large-area, high-resolution DRS imaging. Here, we have reported the first contact-based multipixel DRS imaging system with fiberless illumination of tissue, as well as one in which the size of the detector and aperture as well as the spacing between adjacent channels can be customized. This system demonstrates a nearly 100-fold reduction in size over a previously reported clinically tested bench-top DRS imaging system for breast tumor margin assessment, making it amenable for tumor margin assessment within the space constraints of an operating room. The resolution of the custom imaging array is 4.5 mm compared to 10 mm in the clinically tested multipixel fiber probe [12]. In addition, replacement of the imaging spectrograph (~\$12,000) and cooled CCD array (~\$20,000) [13], with eight discrete wavelength filters (~\$1440), and a custom imaging array (~\$1400) with custom read-out electronics (~\$1000), respectively, has led to an 8-fold reduction in cost compared to the clinically tested bench-top system. Table 2 shows a system level comparison of the reported system to the previously reported bench-top system [12].

Table 2. System level comparison of the clinically tested bench-top system [12] to the system reported herein

System	No. of Wavelengths	Size	Imaging Area	Pixel Spacing	SNR (on Spectralon standard)	Approximate Time to measure a 20 cm ² margin
8-channel Clinical System [12]	81 ($\lambda = 400$ nm to 600 nm)	2 m \times 1.5 m \times 1 m	800 mm ²	10 mm	45.2 dB $\lambda = 450$ nm 39.1 dB $\lambda = 600$ nm	7-8 min.
16-channel Custom Imaging System	8 ($\lambda = 470$ nm to 600 nm)	0.35 m \times 0.3 m \times 0.3 m	256 mm ²	4.5 mm	54.2 dB $\lambda = 470$ nm 52.3 dB $\lambda = 600$ nm (100 ms ITIA integration time)	6 min.

6. Conclusion

For the system reported herein, individual system components for light detection (PD array), light delivery (free-space light delivery tube), and electronic read-out (8-channel ITIA circuit) have been designed, independently optimized, fabricated, and characterized, followed by quantification of system SNR and crosstalk using breast tissue mimicking phantoms. The system SNR was measured to be 35 dB to 45 dB for $\lambda = 470$ nm to 600 nm on benign and cancerous breast tissue mimicking phantoms using two free-space light delivery strategies; a reflective tube that optimized power through PD apertures at the cost of a larger angular distribution of rays, and an absorbing tube that results in lower power throughput but also a smaller angular distribution of rays through the PD apertures. The angular distribution of rays through the PD apertures has implications on the optical crosstalk of the system. Optical crosstalk in tissue was measured on breast tissue mimicking phantoms and was compared for two different light delivery strategies. Forward Monte-Carlo modeling was conducted to

provide a preliminary estimate of system crosstalk, and this model was validated against the measured crosstalk. Longer ITIA integration times (100 ms) and use of an absorbing tube for light delivery resulted in high SNR (36 dB to 48 dB), while minimizing crosstalk (lower than 15%) for an imaging resolution of 4.5 mm.

Acknowledgments

This research was supported by the National Institutes of Health through the Bioengineering Research Partnership award 1 RO1 EB011574-01A1.